Catalysis
Science & Technology

RSC Publishing

PAPER

View Article Online
View Journal

Cite this: DOI: 10.1039/c3cy00198a

Enhancing the performance of SBA-15-supported copper catalysts by chromium addition for the chemoselective hydrogenation of *trans*-cinnamaldehyde

B. Dragoi,*[a] A. Ungureanu,[a] A. Chirieac,[a] V. Hulea,[b] S. Royer[c] and E. Dumitriu[a]

SBA-15-supported copper–chromium mixed oxide nanoparticles (CuCr/SBA-15) were prepared by incipient wetness impregnation followed by mild drying at 25 °C and calcination. The Cu : Cr weight ratios were 1 : 1, 5 : 1, and 10 : 1, at a constant total loading of 5 wt%. Monocomponent SBA-15-supported Cu–oxide (Cu/SBA-15) and Cr–oxide (Cr/SBA-15) were prepared as reference samples. The materials were systematically characterized by XRD at low and high angles, N_2 physisorption, DR UV-vis, FT-IR, and XPS spectroscopies, and TPR. XRD at low angles and N_2 physisorption confirmed the preservation of the mesoporous structure of the SBA-15 support after impregnation and calcination. In the case of monocomponent samples, CuO appeared poorly dispersed, while the Cr species (Cr_2O_3, mono- and polychromates) appeared highly dispersed on the surface of the SBA-15 support. The progressive addition of chromium to copper had positive effects on the average crystallite size of CuO, which decreased from ~28 nm (Cu/SBA-15) to ~3 nm (CuCr/SBA-15; Cu : Cr = 1 : 1), and on reducibility, as well. Metallic active phases were obtained by reducing of the oxide phases under a hydrogen flow at 350 °C. By comparison to the monometallic catalysts, the reduced CuCr/SBA-15 materials were active in the hydrogenation of cinnamaldehyde and chemoselective towards cinnammyl alcohol (>50 mol%). The activity can be correlated with the particle size of copper, whereas the high selectivity to unsaturated alcohol can be associated with the presence of dual Cu^0–Cr^{n+} sites.

Received 24th March 2013,
Accepted 28th May 2013

DOI: 10.1039/c3cy00198a

www.rsc.org/catalysis

Introduction

During the last decades, much attention has been paid to bulk or supported copper catalysts due to their intrinsic activity in many reactions such as toluene oxidation,[1] hydrogenolysis of esters,[2] steam reforming of methanol,[3] water gas shift,[4] dehydrogenation of alcohols,[5,6] hydroamination of alkynes,[7] hydrogenation of cinnamaldehyde[8–12] and so on. Usually, the copper based materials have been prepared by precipitation, chemical vapor deposition and sol–gel synthesis because these methods allow the achievement of high loadings of copper combined with high dispersions and satisfying thermal stability.[13,14] However, some disadvantages of these methods, such as the high toxicity of the precursors and/or the solvents used, or the low activity displayed by the final materials due to the encapsulation of the active phase in the sol–gel catalysts, make them unattractive for the preparation of the copper supported nanoparticles.

In this context, the preparation of the copper supported nanoparticles *via* incipient wetness impregnation seems to be an appropriate alternative due to its simplicity, low cost and lack of waste. However, the main drawback of the method consists of the formation of large particles during the thermal treatments, including the drying step at 120 °C and the calcination at elevated temperatures (generally ranging from 350 to 700 °C). Moreover, the high mobility of the copper species[15] makes them even more difficult to be stabilized on a support. In this context, many efforts are made nowadays to improve the dispersion and thermal stability of the supported copper (oxide) nanoparticles.

A first approach has been reported by de Jong *et al.* and consists of the control of the calcination atmosphere, for instance, the replacement of air with a mixture of 2% NO/N_2.[16] Also, the direct reduction of the supported copper hydroxinitrate proved to be an effective method to get highly

[a] *Gheorghe Asachi Technical University of Iasi, Faculty of Chemical Engineering and Environmental Protection, 71A D. Mangeron Bdv., 700050 Iasi, Romania. E-mail: bdragoi@tuiasi.ro; Fax: +40-232 271311; Tel: +40-232 278683*
[b] *Institut Charles Gerhardt, UMR 5253, CNRS-UM2-ENSCM-UM1, MACS, 8 rue de l'Ecole Normale, 34 296 Montpellier Cedex 5, France*
[c] *Université de Poitiers, CNRS UMR 7285, IC2MP, 4 Rue Michel Brunet, 86022 Poitiers Cedex, France*

dispersed and stable copper nanoparticles but the ammonia generated during the nitrate decomposition still limits its wide application.[16] Toupance *et al*. have reported that the drying of the impregnated hydrated copper nitrate–SiO_2 composite at ambient temperature prevents the agglomeration of the copper hydroxinitrate crystals into larger particles, but the calcination step still generates a broad particle size distribution.[17] Recently, we reported a study on the dispersion and stabilization of copper in CuNi/SBA-15 materials by incipient wetness impregnation followed by gentle drying at 25 °C and calcination under stagnant air. Under these conditions, we demonstrated that both the oxide and the metal nanoparticles display improved dispersion, besides high thermostability during the calcination and reduction steps.[18] It is worth mentioning that the presence of a second metal (*i.e.*, nickel) was an important factor that prevented the sintering and migration of the copper oxide outside the pores. Indeed, extended studies on the role of the chemical composition, *i.e.*, Cu : Ni ratio, on the morphology and structure of the oxide nanoparticles highlighted the positive role of the nickel on the dispersion, stability and reducibility of copper and *vice versa.*[19] These results indicate a synergistic effect between the two metal components that reached a maximum for an optimum Cu : Ni weight ratio of about 1 : 4.

The feasibility of the copper stabilization *via* formation of a solid solution was previously reported by Marchi *et al.*[20] They included copper in ternary and quaternary oxides adopting spinel structures. Accordingly, they observed improved reducibility of the copper cations highly dispersed in the super-stoichiometric zinc aluminate spinel in comparison with copper supported on silica or even a Cu–Al mixed oxide prepared by co-precipitation. Moreover, the authors observed an effect of the second transition metal on the dispersion and reducibility of copper. Therefore, the reduction of copper in the calcined Cu–Ni–Zn–Al took place at T_{max} = 277 °C, while the copper in Cu–Co–Zn–Al sample was reduced at T_{max} = 217 °C. It was also reported that in the binary Cr_2O_3–CuO systems, Cr_2O_3 prevents the agglomeration of the CuO into larger particles.[21,22] However, this promoting effect is still not well understood. It was suggested that this stabilization occurs *via* (a) formation of separated CuO and $CuCr_2O_4$ or (b) Cr_2O_3 acts as an obstacle between CuO crystallites hindering the growing of the larger particles. Accordingly, it was also pointed out that Cr_2O_3 has not only the role of promoter of the copper structure, but also facilitates electron transfer between copper and chromium species, and thus modifies the final properties of the system.

The nature of the solid used as a support for the deposition of metal (oxide) nanoparticles is also a key factor to control the dispersion and stability of the nanoparticles. In this context, the ordered mesoporous silicas such as SBA-15 are of particular interest as host materials for nanoparticles due to their two-dimensional hexagonally arranged channel system, typically of 5–9 nm in mean pore diameter, and large specific surface areas. Recently, Tsoncheva *et al.*[22] reported the deposition of copper–chromium particles on SBA-15 by incipient wetness impregnation technique and acetylacetonate precursors in toluene. They showed that the chemical composition of the samples, as well as the texture of the support, strongly influence the dispersion of the bicomponent particles as well as the formation of the copper–chromium spinel structures. However, the mechanism for the improvement of the copper dispersion in binary Cu–Cr materials still remains unknown.

The interest for the copper–chromium oxides also arises from the great importance of these materials as effective non-precious metal catalysts for CO[23] and VOCs elimination.[24] Moreover, some authors reported that the addition of chromium to copper that was supported on zirconia by impregnation or copper that was deposited on carbon L2S appreciably improved the catalytic performances of the resulting materials in the hydrogenation of α,β-unsaturated aldehydes.[25]

The hydrogenation of cinnamaldehyde (CNA) is a challenge in fine chemicals synthesis due to the presence of conjugated double bonds in the side chain of the phenyl ring, *i.e.*, olefin (C=C) and aldehyde (C=O) bonds. From the thermodynamics point of view, the hydrogenation of the C=C bond with the formation of the hydrocinnamaldehyde (HCNA) is easier to perform while the hydrogenation of the C=O bond requires a chemoselective catalyst to produce the unsaturated alcohol, cinnamyl alcohol (CNOL). Currently, the industrial production of CNOL is centered on three methods: (i) Meerwein–Ponndorf–Verley reduction using aluminium alcoholates as catalysts, (ii) selective hydrogenation of cinnamaldehyde using an alkali borohydride and (iii) to a much lesser extent, the selective hydrogenation using osmium on carbon as a catalyst.[26–28] In this context, researchers are making efforts to find an appropriate heterogeneous catalyst for the selective hydrogenation of cinnamaldehyde with potential applications in industry. So far, a significant number of publications have been generated by academic media, whose importance is still limited to the fundamental research. In the majority of cases noble metals are reported as the most efficient catalysts.[29] Nevertheless, reports on the non-noble metals such as copper or nickel as catalysts for the hydrogenation of CNA have become more frequent in the last few years.[11,12,20,30–32]

Herein, we show that using the incipient wetness impregnation followed by mild drying, a high dispersion of copper–chromium mixed oxide nanoparticles on SBA-15 can be achieved. Accordingly, improved reducibility and catalytic properties are obtained, as compared with the monocomponent counterparts. Mono- and bicomponent CuCr/SBA-15 samples with various Cu : Cr weight ratios were prepared and the oxide forms were characterized to study their chemical composition, texture, particle size and structure, and reducibility. After reduction under hydrogen flow, the catalysts were evaluated in the hydrogenation of cinnamaldehyde, a reaction that is highly sensitive to the properties of the supported bimetallic nanoparticles (*e.g.*, the nature of metals and promoters and their bulk and surface chemical composition, nature of support, and particle morpho-structural properties, in relation to the catalyst preparation method and pretreatment conditions).

Experimental

Materials

All the chemicals required to prepare the support and the catalysts were used without any additional purification: tetraethylorthosilicate

($Si(OC_2H_5)_4$, TEOS, 98%, Aldrich), non-ionic triblock co-polymer Pluronic P123 (poly(ethylene oxide)-*block*-poly(propylene oxide)-*block*-poly(ethylene oxide), $EO_{20}PO_{70}EO_{20}$, molecular weight = 5800, BASF Corp.), copper nitrate ($Cu(NO_3)_2{\cdot}3H_2O$, 98%, Aldrich), chromium nitrate ($Cr(NO_3)_2{\cdot}9H_2O$, 99%, Sigma-Aldrich), distilled water and hydrochloric acid. The chemicals used for the hydrogenation reaction were also used as received: *trans*-cinnamaldehyde (C_6H_5–CH═CH–CHO, 98%, Merck) as reagent and propylene carbonate ($C_4H_6O_3$, 99%, Sigma-Aldrich) as solvent.

Support and catalysts preparation

SBA-15 silica was synthesized following the classical method.[33] The solid was obtained by calcination in air at 500 °C for 6 h with a heating rate of 2.5 °C min^{-1}.

Mono- and bicomponent catalysts were prepared by incipient wetness impregnation method as follows: the freshly calcined SBA-15 support was impregnated with an aqueous solution of the corresponding hydrated nitrates to obtain, assuming that both cations are completely reduced to the metallic phase, a total metal loading of 5 wt%. For the bicomponent samples, three Cu : Cr weight ratios were taken into account, *i.e.*, 1 : 1, 5 : 1, and 10 : 1. All the impregnated materials were submitted to a gentle drying step at 25 °C for 5 days. The oxides of copper and chromium were obtained after calcination under stagnant air at 500 °C for 6 h (heating ramp of 1.5 °C min^{-1}). The monocomponent samples were labeled as M/S, where M = Cu or Cr and S = SBA-15 while the bicomponent samples were labeled as Cu_xCr/S, where x = 1, 5 and 10.

Physico-chemical characterization

All the solid materials were systematically characterized by XRD at low and high angles, nitrogen physisorption, TPR and FT-IR, DR UV-vis, and XPS spectroscopies.

XRD measurements were performed on a Bruker AXS D8 apparatus with monochromatic CuKα radiation (λ = 0.15406 nm wavelength) at room temperature. For small angles analysis, all patterns were recorded over the 2θ range from 0.5 to 6° with a step of 0.01°. For high angle interval, the patterns were recorded from 15 to 80° 2θ with a step of 0.02°. The crystallite sizes of the oxides were calculated by using the Scherrer equation: $d_{hkl} = \lambda/\beta\cos\theta$, where λ = incident ray wavelength (0.15406 nm); β = peak width at half height (rad) after Warren's correction for instrumental broadening, θ = Bragg angle.

Nitrogen physisorption was carried out at 77 K on an Autosorb 1-MP automated gas sorption system (Quantachrome Instruments). Before the analysis, the samples were pretreated as follows: 50 mg of calcined sample was out-gassed under high vacuum at 350 °C for 3 h. After recording the adsorption/desorption isotherms, textural properties were calculated using Autosorb 1 software. The BET surface area, S_{BET}, was assessed using the multipoint BET algorithm for the relative pressure, p/p_o, ranging between 0.10 and 0.30. The total pore volume, V_p, was evaluated at a relative pressure of about 0.975. The micropore volume and the surface of the micropores were evaluated by the *t*-plot method (de Boer statistical thickness = 3.6–8.3 Å). The mesopore size distribution was determined by NLDFT equilibrium algorithm for cylindrical pores.

Temperature programmed reduction was carried out on an Autochem 2910 analyzer from Micromeritics. 100 mg of calcined catalyst was placed in a U-shaped microreactor and activated at 500 °C for 1 h (heating ramp of 15 °C min^{-1}, air flow of 30 mL min^{-1}). After cooling to 50 °C, 3% Ar/H_2 mixture was stabilized at 20 mL min^{-1} flow rate into the sample tube. During the analysis, the temperature was increased up to 900 °C at a rate of 10 °C min^{-1}. The effluent gas was monitored with a TCD.

Diffuse reflectance UV-visible spectra were recorded on a Shimadzu UV-2450 spectrometer equipped with an integrating sphere unit (ISR-2200). The spectra were collected in the range of 200–800 nm and using $BaSO_4$ as a reference.

Infrared spectra were collected on a Vector 22 FT-IR spectrometer from Bruker over the wave number range of 400–4000 cm^{-1}, using pellets formed from a mixture of 99 mg KBr and 1 mg of sample. Each spectrum was obtained by averaging 40 scans with a resolution of 2 cm^{-1}.

XPS spectra were recorded on an ESCALAB 250 (Thermo Electron, Thermo Fisher Scientific, WI) photoelectron spectrometer equipped with a monochromatic Al-Kα source (1486.6 eV, powered at 20 mA and 10 kV). The binding energies were determined relative to the Si 2p XPS peak set at 103.2 eV. Quantification of the elements and their valences was based on a non-linear least squares fitting program using a sum of Lorentzian and Gaussian component curves after background subtraction and using the Scofield coefficients as correction factors.

Hydrogenation of *trans*-cinnamaldehyde

The hydrogenation of *trans*-cinnamaldehyde was performed in liquid phase at atmospheric pressure, in a thermostated three-neck glass reactor equipped with a reflux condenser, hydrogen bubbler and magnetic stirrer. The following reaction conditions were applied: 265 mg of sample that had been reduced in H_2 flow (1 L h^{-1}) at 350 °C for 10 h (heating ramp of 6 C min^{-1}), reaction temperature of 150 °C, 1 mL of CNA, 25 mL of propylene carbonate, hydrogen flow of 1 L h^{-1} and constant stirring speed of 900 rpm to achieve the kinetic regime. Samples were periodically taken off and analyzed by GC (HP5890 equipped with DB-5 capillary column (25 m × 0.20 mm × 0.33 μm) and FID) with the following temperature program: initial temperature of 150 °C (1 min) followed by heating (15 °C min^{-1}) up to 270 °C. The identification of the products was achieved from the retention times of the pure compounds and occasionally by GC-MS (Agilent 6890N system equipped with Agilent 5973 MSD detector and 30 m DB-5 ms column). Quantitative analyses were performed by taking into account the FID response factors for each compound.

Results and discussion

Structural and textural characterization

XRD at high and low 2θ angles. Fig. 1 displays the diffraction patterns collected at high 2θ angles for the chromium and/or

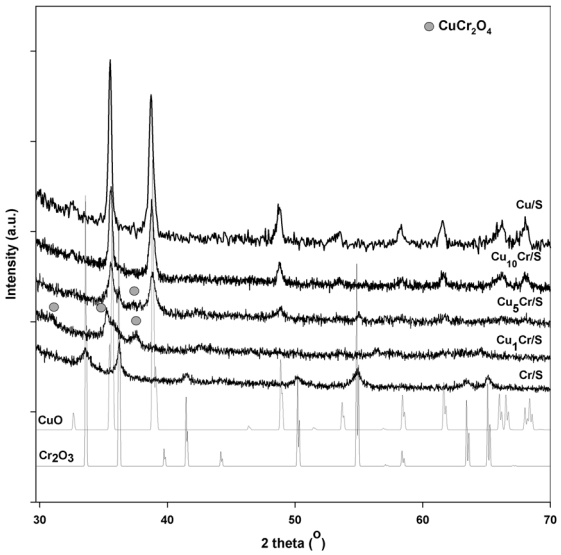

Fig. 1 HA-XRD patterns for the calcined samples.

copper oxides supported on SBA-15. It can be observed that these patterns contain different reflections depending on the sample composition. Therefore, at the same total content in metal (5 wt%), the copper containing sample exhibits reflections characteristic to CuO (tenorite[34]) while the chromium containing sample exhibits typical reflections of Cr_2O_3. Also, it was noted that the peaks of Cr_2O_3 are much less intense and broader than those of CuO, indicating differences in the crystallite sizes for the two oxides. Moreover, the crystallite size as well as the shapes of the peaks give information on the localization of the oxide particles. The average crystallite size evaluated by Scherrer equation shows values of 28 nm for CuO (Table 1) that are much larger than the average pore size of the parent SBA-15 while the reflection peaks at $\sim$35 and $\sim$38° are very intense and thin. These observations suggest a localization of the oxide particles outside of the pores. For Cr_2O_3, the diffraction peaks are not very intense and their lorentzian shape indicates a wide distribution of crystallite size with a maximum at 8.7 nm that is very close to the average pore size (8.5 nm) suggesting that the most part of crystallites are located inside the pores of the SBA-15 silica.

When copper is substituted by chromium, the XRD patterns change as a function of the Cu : Cr ratio. Therefore, the gradual replacing of copper by chromium predominantly leads to a decrease in the intensity of CuO diffraction peaks, while the FWHM value slightly increases in comparison to the Cu/S monocomponent sample, suggesting the formation of smaller CuO particles in the bicomponent samples. The diffraction peaks corresponding to the Cr_2O_3 phase, and easily observed in the monocomponent material, strongly decreased for the bicomponent samples. Additionally, the formation of $CuCr_2O_4$ spinel structure was observed in the bicomponent samples. The intensity of those peaks increases with the amount of chromium in the sample and reached a maximum for the Cu_1Cr/S sample. According to these results, the stabilization of copper seems to occur *via* two routes: (i) the formation of the copper–chromium spinel and (ii) the interposition of Cr_2O_3 between CuO crystallites preventing, thus, the agglomeration of CuO into larger particles.[21,22]

The periodicity of the pore structure in the SBA-15 support and in Cu–Cr containing samples was followed by XRD at low 2θ angles and the collected diffractograms are illustrated in Fig. 2. The pattern of the SBA-15 presents three diffraction peaks at 2θ below 2°, indexed as the (100), (110), and (200) *hkl* reflections typical for a *p6mm* symmetry. The corresponding *d*-spacing of the (100) plane is 9.59 nm and the a_o parameter is 11.08 nm (Table 1). Therefore, the support used to prepare the catalysts is well ordered at long range and contains mesopores in a hexagonal array, as previously described.[33] After the impregnation of the support with nitrate precursors (chromium and copper) and calcination, the typical reflections of SBA-15 were identified in all diffractograms, indicating the preservation of the long-range order of the mesopores upon oxide formation. Nevertheless, it is known that the differences of the electron density distribution are sensitive to the distribution of the matter in the solid.[35,36] Therefore, the electronic

Table 1 Structural and textural properties of the samples

Sample	Cu/(Cu + Cr) (wt ratio)	d_{100}[a] (nm)	a_o[b] (nm)	S_{BET}[c] ($m^2\ g^{-1}$)	S_{micro}[d] ($m^2\ g^{-1}$)	V_p[e] ($cm^3\ g^{-1}$)	V_{micro}[f] ($cm^3\ g^{-1}$)	APS[g] (nm)
SBA-15	—	9.59	11.08	695 (100%)	113	1.11	0.052	8.5
Cu/S	1	9.59	11.08	690 (99%)	109	1.09	0.050	8.5
$Cu_{10}Cr/S$	0.91	9.49	10.96	633 (91%)	88	1.04	0.042	8.5
Cu_5Cr/S	0.84	10.04	11.59	600 (86%)	79	0.98	0.038	8.5
Cu_1Cr/S	0.50	10.15	11.72	606 (87%)	93	0.98	0.045	8.5
Cr/S	0	9.92	11.45	616 (89%)	93	0.99	0.042	8.5

[a] d_{100} = The lattice spacing obtained by low angle XRD. [b] a_0 = The hexagonal unit cell parameter calculated using the equation: $a_0 = 2d_{100}\sqrt{3}$. [c] S_{BET} is the total specific surface area obtained using the BET equation. [d] S_{micro} is the micropore surface area obtained by the *t*-method applied on the linear region of the first part of the isotherm. [e] V_p is the total pore volume measured at $p/p_0 = 0.97$. [f] V_{micro} is the micropore volume obtained by the *t*-method. [g] APS is the average pore size evaluated by NL-DFT for cylindrical pores/equilibrium model.

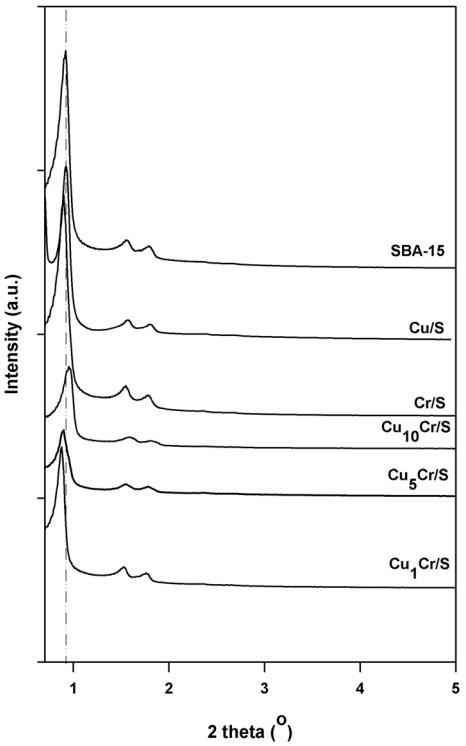

Fig. 2 LA-XRD patterns for the calcined samples.

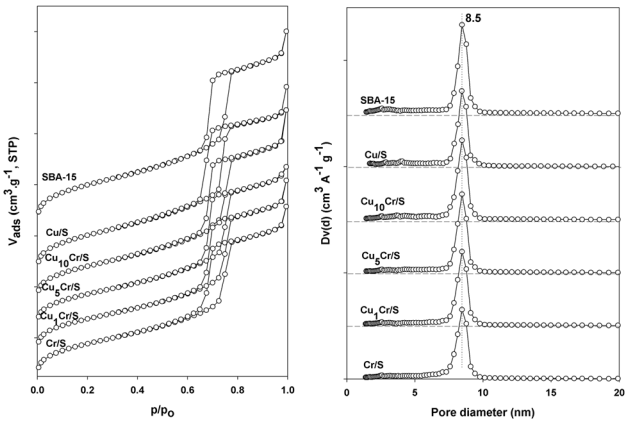

Fig. 3 N_2 physisorption isotherms (left) and pore sizes distribution curves (right) for the calcined samples.

density of the empty pores is equal to the density of air while the electronic density of the walls is higher than that of the air. Accordingly, changes in the electronic density of the pores and/or walls could be observed in the collected diffractograms, more precisely in the intensity of the diffraction peaks as well as their corresponding 2θ values. Indeed, the patterns included in Fig. 2 show small changes in the intensities of the (100) peak. In addition, shifts in 2θ peak position were noticed depending on the composition. The Cu/S sample has a similar XRD pattern and identical a_o parameter (11.8 nm) as the parent SBA-15, suggesting that the most significant part of CuO crystallites are located on the external surface of the silica grains, as already suggested by XRD at high angle. For the Cr/S sample, the intensity of the first reflection does not significantly change in comparison with the parent SBA-15 but a minor shift towards lower 2θ is observed that corresponds to a slight increase in interplanar distance (9.92 nm *vs.* 9.59 nm). Based on these results and the physisorption measurements, the wall thickness was calculated and found to be of 2.95 nm for Cr/S, instead of 2.58 nm for SBA-15.

It seems that the metal precursors introduced in the pores changed the electron density distribution with direct consequences on the reflection intensities as previously proposed by Wang *et al.*[37] Accordingly, the formation of a thin layer of oxide precursors on the internal walls does not significantly change the intensity of the first reflection in comparison with the parent SBA-15. Moreover, a spatial order could be responsible for an increased intensity in comparison with that of the parent support. By contrast, when impregnated species are chaotically oriented inside the pores, they practically fill the pores and, thus, the electronic density of the pores is higher than air. In this case, the intensity of the (100) peaks is diminished. If the results of XRD at high angles are considered, which show very small Cr_2O_3 crystallites probably grown inside the pores, the formation of a very thin film of chromium oxide species on the internal surface of the mesopores might be admitted, due to the absence of a significant (100) peak intensity decrease.

N_2 physisorption. The porosity of the samples was further characterized by nitrogen physisorption at 77 K. The N_2 physisorption isotherms and pore size distribution curves of the samples are shown in Fig. 3. Details of the textural properties derived from these isotherms are summarized in Table 1. The isotherm of the parent SBA-15 is of type IV according to IUPAC classification and it reflects the mesoporous structure also being in good agreement with the XRD pattern recorded at low 2θ angles.[33] The single step capillary condensation at relative pressure, $p/p_o = 0.73$, reflects the presence of cylindrical mesopores with a narrow pore size distribution (PSD). The maximum of the PSD curve is centered at 8.5 nm and represents the average pore size of the sample. The surface area of the Cu/S sample is close to that of the parent SBA-15, indicating no significant changes on the internal surface of this sample and sustaining the XRD results, which stand for the external localization of the CuO particles. After impregnation with nitrates of copper and/or chromium and calcination, the shape of the nitrogen physisorption isotherms did not change, the capillary condensation taking place at the same relative pressure as for the SBA-15 support. Hence, the pore size distribution curves exhibit the same maximum at 8.5 nm.

These general observations indicate the absence of any structural collapse of the ordered mesophase during the impregnation of the SBA-15 and subsequent thermal treatments (*i.e.*, drying and calcination). Also, no delay on the desorption branch was identified in any of the isotherms, which points out that the principal mesopores remain open, and that no significant constriction forms in the pores after calcination. However, the decreases in specific surface areas and pore volumes suggest the localization of the oxides precursors inside the mesopores of the SBA-15.

Spectroscopic investigation

DR UV-vis spectroscopy. First information on the metal oxides species generated by calcination of the copper and chromium nitrates impregnated on SBA-15 was provided by DR UV-vis spectroscopy. The spectra are illustrated in Fig. 4.

The spectrum of the Cu/S sample presents two distinct absorption bands: (i) a LMCT (ligand-to-metal-charge-transfer) band with a maximum at 250 nm and (ii) a very broad absorption band at 360–800 nm. The first low intense band, due to $O^{2-} \rightarrow Cu^{2+}$ LMCT in octahedral coordination of Cu^{2+}, is associated with a minor population of Cu^{2+} in highly dispersed CuO.[38] The second band represents overlapped absorptions coming from Cu^{2+} in a variety of CuO species usually found in bulk CuO particles for example, Cu–O–Cu oligomers, low-symmetry Cu species such as square-planar CuO_x, and Cu^{2+} ions in a distorted octahedral environment caused by the Jahn–Teller effect.[38] The spectrum of the Cr/S sample contains several well-resolved absorption bands with maxima at 270, 350, 460 and 600 nm.

These bands characterize several chromium species, although only Cr_2O_3 was detected by XRD. The other chromium species are either present in a low amount or remain amorphous, avoiding their detection by XRD. According to previous works on chromium supported on different supports (*i.e.*, silica, SBA-15, MCM-41, Al_2O_3), different chromium species (*i.e.*, Cr^{6+} and Cr^{3+}) were generated depending on the chromium amount and the nature of the support.[22,39–46] Cr^{6+} is usually found tetrahedrally coordinated by oxygen in CrO_3, $[CrO_4]^{2-}$ and $[Cr_2O_7]^{2-}$, while Cr^{3+} is found in distorted octahedrally coordinated environments such as in Cr_2O_3. Based on these studies, the absorption bands identified in the spectrum of the Cr/S sample at 270 and 350 nm are attributed to $O^{2-} \rightarrow Cr^{6+}$ LMCT transitions in highly dispersed Cr^{6+} in tetrahedral coordination. The bands at 460 and 600 nm are attributed to d–d transitions of Cr^{3+} in octahedral symmetry. Therefore, the DR UV-vis spectroscopy revealed the simultaneous formation of mono- and polychromate species of Cr^{6+} and Cr_2O_3 (Cr^{3+}), the last one already being identified by XRD.

The spectra collected for the bicomponent samples contain similar absorption bands as for the monocomponent counterparts. However, the intensities of the bands as well as the blue or red shifts depend on the amount of each element as well as their dispersion on the SBA-15 surface. The first absorption band was observed at 250 nm ($Cu_{10}Cr/S$) and 260 nm (Cu_5Cr/S and Cu_1Cr/S), respectively while a second band was observed at 360 nm for all bicomponent samples. These bands are assigned to highly dispersed copper and chromium (mainly Cr^{6+}) species, probably interacting together. The intensities of the absorption bands between 400 and 600 nm are diminished in comparison with the monocomponent samples and they are attributed to Cu^{2+} and Cr^{3+} in CuO, Cr_2O_3, and $CuCr_2O_4$ spinel. The absorption band with the maximum at ~760 nm slowly increases with the amount of copper and is assigned to d–d transitions of Cu^{2+} ions in octahedral coordination geometries in CuO particles.

FT-IR spectroscopy. The further investigation of the oxide species were performed by analyzing the vibrational spectra collected for the chromium containing samples and illustrated in Fig. 5.

Due to the presence of the silica support, these spectra show contributions of both the silica and the metal oxides supported on the silica. Therefore, the infrared bands specific to the silica framework (*i.e.*, 1200, 1100, 812 and 470 cm^{-1}) are not discussed herein.[39] Supplementary bands were identified at 560, 625 and 920 cm^{-1}. Interestingly, the intensities of all these

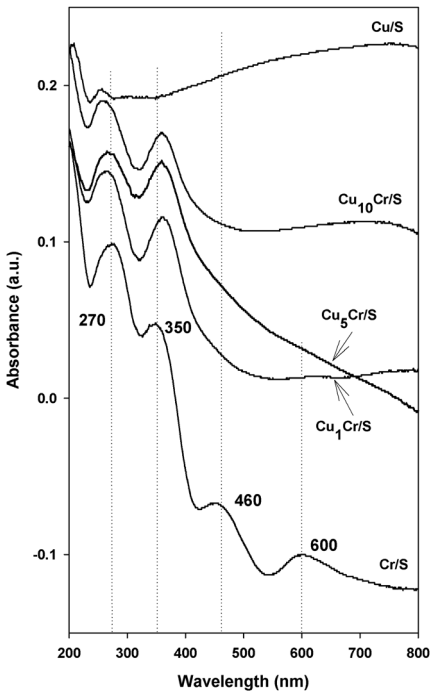

Fig. 4 DR UV-vis spectra for the calcined samples.

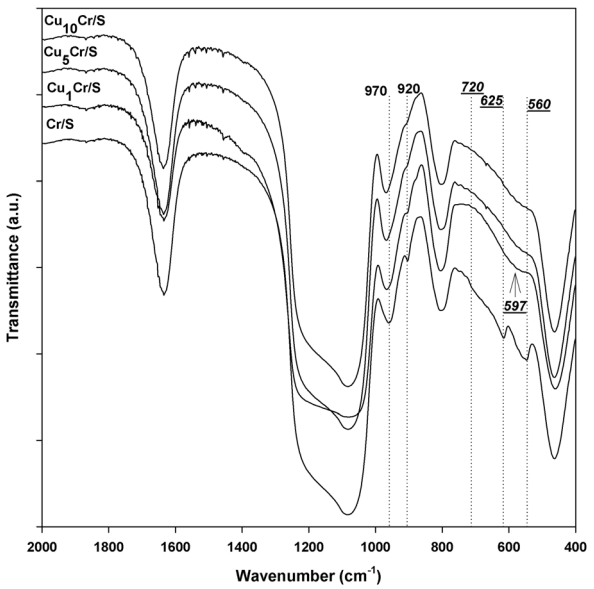

Fig. 5 FT-IR spectra for the calcined samples.

bands decrease as the amount of chromium decreases, and they are therefore considered as ''fingerprints'' of the chromium species. The vibration bands observed at 560, 625 and the shoulder at 720 cm^{-1} in the Cr/S sample originate from Cr–O vibration in crystalline Cr_2O_3.[47,48] For the bicomponent samples, the band at 560 cm^{-1} is shifted to 597 cm^{-1} and is attributed to the chromite anion.[49] This is in good agreement with XRD data showing the formation of $CuCr_2O_4$, especially for the samples with a high amount of chromium (Cu_5Cr/S and Cu_1Cr/S). As concerns the absorption at 920 cm^{-1}, it might correspond to Cr═O stretching vibrations of mono- and polynuclear surface chromates.[50]

All the spectra contain a vibration band at around 970 cm^{-1}. It can be observed that the absorption is blue shifted as the amount of chromium decreases in the sample, so that for the $Cu_{10}Cr/S$ the band is observed at 977 cm^{-1}. Due to the dual composition of the samples, *i.e.*, silica–metal oxides, the attribution of this band is more difficult. Usually, this band is observed at 950–970 cm^{-1}, more often at 960 cm^{-1}, and is attributed to the stretching vibration of free silanols on the silica surface. Frequently, the same band was attributed to Si–O stretching vibration in the Si–OR group, where R = Ti,[51–55] Cr,[56] or Cu.[57] In accord with these results, the band observed at ~970 cm^{-1} is attributed to Si–O–Cr vibrations. Additionally, it was observed that the shift to higher wave numbers of this band is proportional to the increase in copper amount. Therefore, this band could be a contribution of the two metals (*i.e.*, copper and chromium) interacting with the silica surface.

XPS analysis. The surface composition in the copper and chromium containing materials was investigated by XPS analysis. The binding energies (BE) besides the valence state assignment and atomic surface composition are listed in Table 2.

Two oxidation states were observed for chromium in the Cr/S sample, with BE of 576.40 eV and 578.83 eV. According to the literature, these energies are related to Cr^{3+} and Cr^{6+}, respectively.[58–63] This result is in agreement with XRD, FT-IR and DR UV-vis data, all indicating the presence of crystalline Cr_2O_3 as well as species of amorphous Cr^{6+} (such as CrO_3, $[CrO_4]^{2-}$ and $[Cr_2O_7]^{2-}$, or even $[Cr_nO_{3n+1}]^{2-}$). Moreover, surface quantification shows that the majority of chromium exists as Cr_2O_3 (68.5% – Table 2) while the Cr/Si ratio (0.020 from XPS *vs.* 0.140 from ICP) indicates that only a small part of the chromium is found in the near surface region.

In the bicomponent samples, a change in the BE of Cr^{6+} was observed in comparison with the Cr/S monocomponent sample. Such a BE shift indicates a change in the chemical environment of the Cr^{6+} cations, which can be attributed to the presence of copper in close interaction. However, this shift of the binding energy remains very limited, irrespective of the copper content. In addition, the relative part of Cr^{6+} is constantly increasing from 31.5% (Cr/S) to 100% ($Cu_{10}Cr/S$), while the contribution of Cr^{3+} (as Cr_2O_3 and $CuCr_2O_4$ according to XRD) decreases from 68.5% (Cr/S sample) to 0% ($Cu_{10}Cr/S$). Additionally, the chromium surface concentration (see Cr/Si ratio in the Table 2) is progressively decreasing with the total amount of chromium in the material.

For copper, BE from 934.25 to 933.66 eV, with a shake-up peak at 942.20 eV, were observed. According to the literature, these energy values depend on the sample composition, crystallinity, and particularly on the copper micro-environment.[1,64–67] For instance, the BE for bulk CuO is 932.4 eV.[68] Accordingly, the decrease in the binding energy from 934.25 eV to 933.6 eV can arise from the decrease in CuO dispersion with the increase in copper content, which is in good agreement with the XRD results. Unlike chromium, the quantitative data listed in Table 2 show that the amount of copper (Cu/Si) in ~10 nm depth from the surface decreases when the amount of copper increases. However, the measured values indicate that a significant part of the copper is located deep inside the samples, and is not visible by XPS.

The XPS results thus confirmed the formation of different copper and chromium oxides species, those distributions at the surface are depending on the composition of the sample. Therefore, a Cu : Cr weight ratio of 1 : 1 is favorable for the formation of copper–chromite spinel while a ratio of 10 : 1 generates only hexavalent chromium species. Moreover, it was

Table 2 XPS data from fitting of Cr 2p and Cu 2p and the surface composition of samples

	Cr $2p_{3/2}$		Cu $2p_{3/2}$		At%		Cr/Si		Cu/Si	
Sample	B.E. (eV)	VSA[a]	B.E. (eV)	VSA[a]	Cr	Cu	ICP	XPS	ICP	XPS
$Cu_{10}Cr/S$	579.07	Cr^{6+}	933.66 942.20	Cu^{2+}	0.08 (100%)	0.14	0.013	0.003	0.139	0.005
Cu_5Cr/S	576.36 579.34	Cr^{3+} Cr^{6+}	934.05 942.20	Cu^{2+}	0.03 (21%) 0.11 (79%)	0.17	0.024	0.007	0.124	0.009
Cu_1Cr/S	576.41 579.21	Cr^{3+} Cr^{6+}	934.25 942.20	Cu^{2+}	0.12 (40%) 0.17 (60%)	0.17	0.069	0.010	0.071	0.012
Cr/S	576.40 578.73	Cr^{3+} Cr^{6+}	—	—	0.39 (68.5%) 0.18 (31.5%)	—	0.140	0.02	—	—

[a] Valence state assignment.

shown that a good dispersion of CuO can be achieved regardless of the Cu : Cr ratio. Accordingly, a positive effect of the Cr^{6+} species on the CuO dispersion could be also assumed.

Reducible properties of the samples

The degree of interaction between the support and the metallic species, as well as metal–metal interactions, was further investigated by TPR. The recorded TPR profiles for the monocomponent and bicomponent samples are displayed in Fig. 6. The TPR curve for the Cu/S sample contains a main reduction peak centered at 345 °C and a shoulder at 500 °C. Normally, these two maxima should correspond to the reduction of Cu^{2+} to Cu^0. Because the XRD results have already shown the presence of large crystalline CuO in the calcined Cu/S sample, for this sample the peak centered at 345 °C can be attributed to the reduction of poorly dispersed CuO. The shoulder identified at 500 °C is not usual for CuO reduction. This peak was observed during the reduction of Cu/MCM-48, and copper in mesoporous silica–alumina, and was attributed to difficult to reduce copper species such as copper silicate.[69–71] Indeed, Van Der Grift *et al.*[72] performed TPR analysis on different copper hydrosilicates and they identified varying reducible behavior for copper species depending on the composition and structure of the silicate. For example, they observed a reduction temperature of 527 °C for dioptase ($CuSiO_2(OH)_2$).

Our results thus evidence the possibility to stabilize a part of the copper in the silica matrix as copper silicate, obtained only by gentle drying of the samples after wetness impregnation of the nitrate precursors.

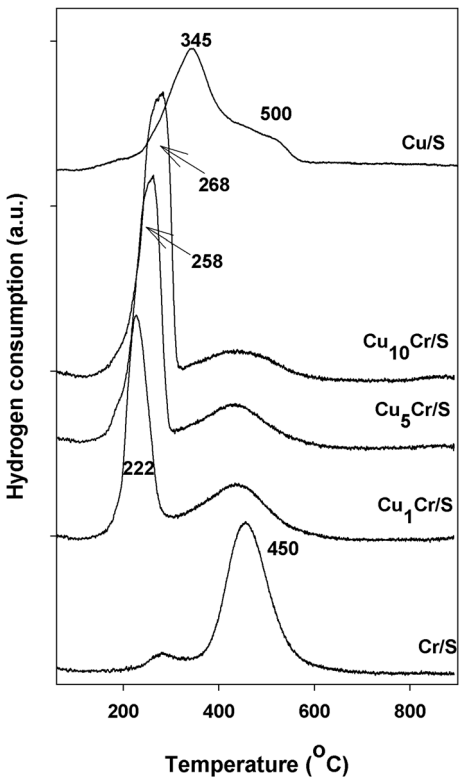

Fig. 6 TPR profiles for the calcined samples.

The TPR curve for the Cr/S sample shows a minor reduction peak at 270 °C and a major one at 450 °C, which may be attributed to the reduction of Cr^{6+} to Cr^{3+}.[43,73–80] It is worth mentioning that the complete reduction of chromium to zero valent chromium is not possible in the TPR experimental conditions.[81,82]

For the bicomponent samples, the TPR profiles contain two main reduction peaks attributed to the reduction of Cu^{2+} to Cu^0 and Cr^{6+} to Cr^{3+}, respectively. It can be noticed that the reduction temperatures of the copper cations shifted to much lower values in comparison with the monocomponent sample (Cu/S). It is known that in the case of CuO, the temperature of reduction is strongly influenced by the particle size and dispersion, *i.e.*, the reducibility is improved when the dispersion is high.[83–85] As revealed by XRD, the bicomponent samples also contain $CuCr_2O_4$ spinels. Therefore, the reduction maxima at 222, 258, and 268 °C for Cu_1Cr/S, Cu_5Cr/S, and $Cu_{10}Cr/S$, respectively have contributions from two precursors, *i.e.* the reduction of Cu^{2+} in highly dispersed CuO and Cu^{2+} in spinel structure, respectively. Thus, the temperatures of copper oxide reduction, which are lower than for the monocomponent material, indicate an interaction between copper species and chromium species in close proximity to each other. For the Cr^{6+} cations, no significant change of the reducibility was observed showing that the oxides interaction only affects Cu^{2+} reducibility.

The physico-chemical characterization discussed above clearly shows that the addition of chromium to copper deposited on SBA-15 has a positive effect on the dispersion and reducibility of copper. Moreover, according to these results, the observed effects also depend on the amount of chromium introduced in the sample. Therefore, a smaller amount of chromium (*i.e.*, Cu : Cr = 10 : 1) favors the stabilization of copper probably *via* a Cr_2O_3 barrier between CuO particles that does not allow the sintering of the CuO into larger particles. Equal amounts of copper and chromium in the sample (*i.e.*, Cu : Cr = 1 : 1) allow the stabilization of copper *via* formation of $CuCr_2O_4$ spinel, as well. Accordingly, the reducibility of copper is much improved as shown above. Taking into account the sensitivity of the hydrogenation of cinnamaldehyde to the properties of the catalyst, these observed structural and reducible effects were evaluated in this reaction and the obtained results are discussed further on.

Calcined Cu–Cr/SBA-15 materials as catalytic precursors for the hydrogenation of *trans*-cinnamaldehyde

After reduction at 350 °C under H_2 flow, the catalytic performances of the Cu_xCr/S materials were evaluated in the hydrogenation of cinnamaldehdye (CNA). According to Scheme 1, the hydrogenation of this aldehyde involves parallel and consecutive reactions. The parallel reactions (1 and 2) lead to the partial hydrogenated products, cinnamyl alcohol (CNOL) and hydrocinnamaldehyde (HCNA), respectively, whose further hydrogenation

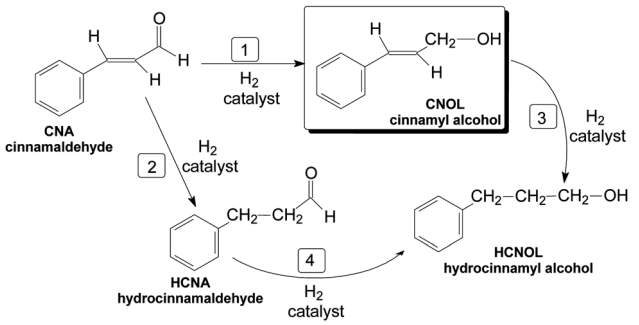

Scheme 1 Reaction pathways for the hydrogenation of CNA.

generates the completely hydrogenated product, hydrocinnamyl alcohol (HCNOL).

It is already accepted that the catalytic activity and selectivity in the hydrogenation of cinnamaldehyde is governed by the competition between the two double bonds during the molecule chemisorption on the catalyst surface. Therefore, the nature and number of the catalytic active sites as well as their microenvironment are the key factors that control the adsorption mode of the CNA molecule, and consequently the selectivities in reaction. First, when the hydrogenation of CNA was performed over the monocomponent samples, *i.e.*, Cu/S and Cr/S, an extremely low activity (below 1.5 mol% after 360 min of reaction, Cu/S) or even the lack of catalytic activity (Cr/S) were noted. Generally, copper is not active in hydrogenation reactions due to its fully occupied d_{10} orbitals. However, when the particles are sufficiently small and highly dispersed, the electronic density increases making copper an active catalyst.[19,29,31] As expected, the Cu/S sample, containing large particles of the Cu species, exhibited very low activity in the CNA hydrogenation. For the Cr/S sample, as the TPR results indicated, it is difficult to reduce chromium oxides to Cr^0. Therefore, the dissociative chemisorption of hydrogen, a prerequisite to the CNA hydrogenation, cannot be accomplished.

When both elements, copper and chromium precursors, are supported on the SBA-15 silica, the reduced materials become active in the hydrogenation of CNA. Fig. 7 displays the typical evolution of the CNA conversion for the mono- and bimetallic Cu_xCr/S catalysts while Fig. 8 illustrates the conversion of CNA *vs.* reaction time as well as the evolution of the products for the Cu_1Cr/S catalyst.

The introduction of a small amount of chromium in the sample ($Cu_{10}Cr/S$) was favorable to the catalytic activity (Fig. 7). Thus, CNA conversion of about 5 mol% was obtained and this is in line with the TPR results, which show the higher reducibility for Cu^{2+} cations in this material. A further increase in chromium content (Cu_5Cr/S), generated a catalyst with a higher activity (~8 mol% of CNA conversion after 360 min of reaction), despite the lower copper content. When copper and chromium are in equal amounts (Cu_1Cr/S) the activity is further improved (~11 mol% of CNA conversion after 360 min of reaction). This behavior is probably due to the initial copper dispersion and reducibility for these samples (according to XRD and TPR results). As concerns the products distribution,

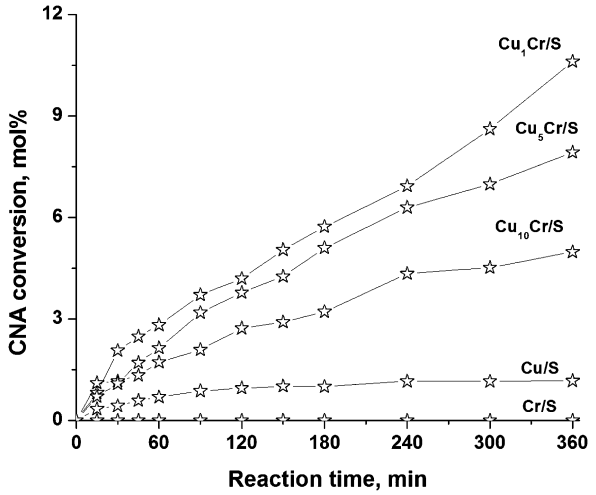

Fig. 7 Typical evolution of CNA conversion *vs.* reaction time for the mono- and bimetallic Cu_xCr/S catalysts (test conditions: $T_{reaction}$ = 150 °C, 0.264 g catalyst, 1 mL of CNA, solvent = propylene carbonate (25 mL), H_2 flow = 1 L h^{-1}, stirring rate = 900 rpm. The full lines represent the reaction products while the dotted lines correspond to CNA conversion).

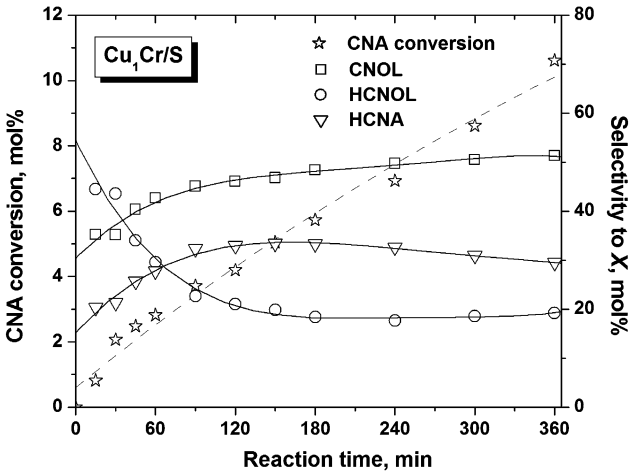

Fig. 8 CNA conversion *vs.* reaction time and the evolution of the reaction products over time with the Cu_1Cr/S catalyst reduced at 350 °C.

the reaction is mainly directed to CNOL (~50 mol%) as illustrated for the Cu_1Cr/S sample (Fig. 8). Note that this value is higher than that previously reported for catalysts containing Cu^0 or Cu^+ species (30 mol%).[10] For all three catalysts, the selectivity to HCNA reached a maximum of ~38 mol%, which thereafter slowly decreased while the HCNOL increased. These trends indicate that similar active sites exist in all samples, on which the adsorption of the two double bonds (C=C and C=O) takes place in the same manner. The higher selectivity to CNOL can be considered as an evidence of the preferred C=O adsorption on the catalyst surface. An explanation for this preferred C=O adsorption on active sites can be given based on the theoretical study of Delbecq and Sautet.[86] According to their theory, it is possible to improve the selectivity to the unsaturated alcohol either by activation of the C=O group or

by hindering the adsorption *via* the C=C bond. The activation of the carbonyl bond is based on the theory of the two-electron stabilizing interactions and involves the addition of an electropositive metallic cation in the close vicinity of the catalytically active metal. This second metallic cation, acting as an acid Lewis site, is an electrophilic center that will attract the free electrons of the oxygen allowing the hydrogenation of the C=O bond. For the Cu–Cr catalysts synthesized in this study, the partially reduced chromium cations (Cr^{3+} and/or Cr^{2+}) are acting as electrophilic sites, which favors the formation of the unsaturated alcohol. Accordingly, the CNA molecules are adsorbed linearly on the cationic Cr^{n+} sites and, thus, the hydrogenation of the C=O bond is achieved by the activated hydrogen on the neighboring Cu^0 (the Cu^0–Cr^{n+} dual sites).

Conclusions

The use of chromium as a second metal positively influences the dispersion of CuO particles and their reducibility, when supported on SBA-15. Two mechanisms were taken into account to explain these results: (i) the formation of copper–chromite spinel and (ii) the interposition of Cr_2O_3 or even Cr^{6+} species between CuO crystallites, preventing thus their aggregation and the formation of bulky particles. The stabilizing effect of chromium was further confirmed by the evolution of catalytic activity on copper–chromium samples in the hydrogenation of cinnamaldehye. Therefore, CNA conversions up to 12 mol% and selectivities to CNOL of ~50 mol% were noted for CuCr/SBA-15, whereas the monocomponent samples showed negligible activity. This high level of chemoselectivity was explained by the existence of dual Cu^0–Cr^{3+}/Cu^0–Cr^{2+} active-adsorption sites, which favor the adsorption of CNA molecules *via* the C=O bond.

Acknowledgements

B. Dragoi acknowledges the project PERFORM-ERA ''Postdoctoral Performance for Integration in the European Research Area'' (ID-57649), financed by the European Social Fund-Romanian Government. The Romanian authors acknowledge the project PN-II-ID-PCE-2011-3-0868, nr. 264/2011 financed by UEFISCDI – Romania.

References

1 M.-J. Suh and S.-K. Ihm, *Top. Catal.*, 2010, **53**, 447.
2 L. Chen, P. Guo, L. Zhu, M. Qiao, W. Shen, H. Xu and K. Fan, *Appl. Catal., A*, 2009, **356**, 129.
3 S. Velu, K. Suzuki, M. Okazaki, M. P. Kapoor, T. Osaki and F. Ohashi, *J. Catal.*, 2000, **194**, 373.
4 T. P. Maniecki, P. Mierczyski and W. K. Jowiak, *Kinet. Catal.*, 2010, **51**, 843.
5 J. N. Keuler, L. Lorenzen and S. Miachon, *Appl. Catal., A*, 2001, **218**, 171.
6 F.-W. Chang, W.-Y. Kuo and K.-C. Lee, *Appl. Catal., A*, 2003, **246**, 253.
7 G. V. Shanbhag, T. Joseph and S. B. Halligudi, *J. Catal.*, 2007, **250**, 274.
8 J. Barrault, A. Derouault, G. Courtois, J. M. Maissant, J. C. Dupin, C. Guimon, H. Martinez and E. Dumitriu, *Appl. Catal., A*, 2004, **262**, 43.
9 M. Chatterjee, T. Iwasaki, Y. Onodera, H. Hayashi, Y. Ikushima, T. Nagase and T. Ebina, *Appl. Clay Sci.*, 2004, **25**, 195.
10 S. Valange, A. Derouault, J. Barrault and Z. Gabelica, *J. Mol. Catal. A: Chem.*, 2005, **228**, 255.
11 V. S. Gutiérrez, A. S. Diez, M. Dennehy and M. A. Volpe, *Microporous Mesoporous Mater.*, 2011, **141**, 207.
12 V. Gutierrez, M. Alvarez and M. A. Volpe, *Appl. Catal., A*, 2012, **413**, 358.
13 W. V. Knowles, M. O. Nutt and M. S. Wong, in *Catalyst Preparation, Science and Engineering*, ed. J. Regalbuto, CRC Press, Boca Raton, 2007, p. 254.
14 J. R. Creighton and P. Ho, in *Chemical vapor Deposition*, ed. J.-H. Park and T. S. Sudarshan, Surface Engineering Series, ASM International, 2001, vol. 2, p. 13.
15 A. Carrero, J. A. Calles and A. J. Vizcaino, *Appl. Catal., A*, 2007, **327**, 82.
16 P. Munnik, M. Wolters, A. Gabrielsson, S. D. Pollington, G. Headdock, J. H. Bitter, P. E. de Jongh and K. P. de Jong, *J. Phys. Chem. C*, 2011, **115**, 14698.
17 T. Toupance, M. Kermarec and C. Louis, *J. Phys. Chem. B*, 2000, **104**, 965.
18 A. Ungureanu, B. Dragoi, A. Chirieac, S. Royer, D. Duprez and E. Dumitriu, *J. Mater. Chem.*, 2011, **21**, 12529.
19 A. Ungureanu, B. Dragoi, A. Chirieac, C. Ciotonea, S. Royer, D. Duprez, A. Sophie Mamede and E. Dumitriu, *ACS Appl. Mater. Interfaces*, 2013, **5**, 3010.
20 A. J. Marchi, D. A. Gordo, A. F. Trasarti and C. R. Apesteguia, *Appl. Catal., A*, 2003, **249**, 53.
21 M. Wojciechowska, J. Haber, S. Łomnicki and J. Stoch, *J. Mol. Catal. A: Chem.*, 1999, **141**, 155.
22 T. Tsoncheva, M. Järn, D. Paneva, M. Dimitrov and I. Mitov, *Microporous Mesoporous Mater.*, 2011, **137**, 56.
23 R. Prasad and P. Singh, *Catal. Rev. Sci. Eng.*, 2012, **54**, 224.
24 A. Z. Abdullah, M. Z. A. Bakar and S. Bhatia, *J. Hazard. Mater.*, 2006, **129**, 39.
25 Z. Ferhat, A. Derouault, J. Barrault and M. Bettahar, *React. Kinet. Catal. Lett.*, 2002, **76**, 249.
26 S. H. Liu, S. Jaenicke and G. K. Chuah, *J. Catal.*, 2002, **206**, 321.
27 H. Surburg and J. Panten, *Common Fragrance and Flavor Materials, Preparation, Properties and Uses*, Wiley-VCH VerlagGmbH & Co. KGaA, Weinheim, 2006, p. 111.
28 A. Y. Hammoudeh, S. M. Saada and S. S. Mahmoud, *Jordan J. Chem.*, 2007, **2**, 53.
29 P. Maki-Arvela, J. Hajek, T. Salmi and D. Y. Murzin, *Appl. Catal., A*, 2005, **292**, 1.
30 H. Wang, Y. Shu, M. Zheng and T. Zhang, *Catal. Lett.*, 2008, **124**, 219.
31 B. Dragoi, A. Ungureanu, D. Meloni, M. Casula, A. Chirieac, A. Sasu, V. Solinas and E. Dumitriu, *Environ. Eng. Manage. J.*, 2010, **9**, 1203.

32 A. Chirieac, B. Dragoi, A. Ungureanu, A. Moscu Corcodel, C. Rudolf, A. Sasu and E. Dumitriu, *Environ. Eng. Manage. J.*, 2012, **11**, 47.
33 D. Zhao, J. Feng, Q. Huo, N. Melosh, G. H. Fredrickson, B. F. Chmelka and G. D. Stucky, *Science*, 1998, **279**, 548.
34 http://database.iem.ac.ru/mincryst/s_carta.php?TENORITE.
35 W. Schmidt, *Microporous Mesoporous Mater.*, 2009, **117**, 372.
36 M. Imperor-Clerc, D. Bazin, M.-D. Appay, P. Beaunier and A. Davidson, *Chem. Mater.*, 2004, **16**, 1813.
37 Y. M. Wang, Z. Y. Wu and J. H. Zhu, *J. Solid State Chem.*, 2004, **177**, 3815.
38 J. J. Bravo-Suárez, B. Subramaniam and R. V. Chaudhari, *J. Phys. Chem. C*, 2012, **116**, 18207.
39 M. I. Zaki, N. E. Fouad, J. Leyrer and H. Knozinger, *Appl. Catal.*, 1986, **21**, 359.
40 M. Casalboni, V. Ciafardone, G. Giuli, B. Izziy, E. Paris and P. Prosposito, *J. Phys.: Condens. Matter*, 1996, **8**, 9059.
41 E. Rombi, M. G. Cutrufello, V. Solinas, S. De Rossi, G. Ferraris and A. Pistone, *Appl. Catal., A*, 2003, **251**, 255.
42 P. Michorczyk, J. Ogonowski, P. Kustrowski and L. Chmielarz, *Appl. Catal., A*, 2008, **349**, 62.
43 L. Zhang, Y. Zhao, H. Dai, H. He and C. T. Au, *Catal. Today*, 2008, **131**, 42.
44 T. Tsoncheva and E. Sarkadi-Priboczki, *Microporous Mesoporous Mater.*, 2012, **148**, 1.
45 M. Popova, Á. Szegedi, Z. Cherkezova-Zheleva, A. Dimitrova and I. Mitov, *Appl. Catal., A*, 2010, **381**, 26.
46 V. R. Elias, E. V. Sabre, E. L. Winkler, M. L. Satuf, E. Rodriguez-catellon, S. G. Casuscelli and G. A. Eimer, *Microporous Mesoporous Mater.*, 2012, **163**, 85.
47 S. M. El-Sheikh, R. M. Mohamed and O. A. Fouad, *J. Alloys Compd.*, 2009, **482**, 302.
48 M. Aghaie-Khafri and M. H. Kakaei Lafdani, *Powder Technol.*, 2012, **222**, 152.
49 E. A. Campos, R. C. L. Dutra, L. C. Rezende, M. F. Diniz, W. M. D. Nawa and K. Iha, *J. Aerosp. Technol. Manage.*, 2010, **2**, 323.
50 D. L. Hoang, A. Dittmar, M. Schneider, A. Trunschke, H. Lieske, K.-W. Brzezinka and K. Witke, *Thermochim. Acta*, 2003, **400**, 153.
51 B. S. Uphade, Y. Yamada, T. Akita, T. Nakamura and M. Haruta, *Appl. Catal., A*, 2001, **215**, 137.
52 W. Y. Jung, S. H. Baek, J. S. Yang, K.-T. Lim, M. S. Lee, G.-D. Lee, S. S. Park and S.-S. Hong, *Catal. Today*, 2008, **131**, 437.
53 N. Phonthammachai, M. Krissanasaeranee, E. Gulari, A. M. Jamieson and S. Wongkasemjit, *Mater. Chem. Phys.*, 2006, **97**, 458.
54 J. C. van der Waal and H. van Bekkum, *J. Mol. Catal. A: Chem.*, 1997, **124**, 137.
55 A. Ungureanu, D. Trong On, E. Dumitriu and S. Kaliaguine, *Appl. Catal., A*, 2003, **254**, 203.
56 K.-T. Li and W.-T. Weng, *J. Taiwan Inst. Chem. Eng.*, 2009, **40**, 48.
57 V. S. Garcia-Cuello, L. Giraldo and J. C. Moreno-Pirajan, *J. Chem. Eng. Data*, 2011, **56**, 1167.
58 G. Pantaleo, L. F. Liotta, A. M. Venezia, G. Deganello,b, E. M. Ezzo, M. A. El Kherbawi and H. Atia, *Mater. Chem. Phys.*, 2009, **114**, 604.
59 B. Liu and M. Terano, *J. Mol. Catal. A: Chem.*, 2001, **172**, 227.
60 A. B. Gaspar, C. A. C. Perez and L. C. Dieguez, *Appl. Surf. Sci.*, 2005, **252**, 939.
61 L. Zhang, J. Deng, H. Dai and C. T. Au, *Appl. Catal., A*, 2009, **354**, 72.
62 M. Gomez-Cazalilla, A. Infantes-Molina, J. Merida-Robles, E. Rodrıguez-Castellon and A. Jimenez-Lopez, *Energy Fuels*, 2009, **23**, 101.
63 V. R. Elías, E. V. Sabre, E. L. Winkler, M. L. Satuf, E. Rodriguez-Castellón, S. G. Casuscelli and G. A. Eimer, *Microporous Mesoporous Mater.*, 2012, **163**, 85.
64 L. Xiaowei, S. Mingmin, H. Xi, Z. Haiyang, G. Fei, K. Yan, D. Lin and C. Yi, *J. Phys. Chem. B*, 2005, **109**, 3949.
65 H. Zhu, Y. Wu, X. Zhao, H. Wan, L. Yang, J. Hong, Q. Yu, L. Dong, Y. Chen, C. Jian, J. Wei and P. Xu, *J. Mol. Catal. A: Chem.*, 2006, **243**, 24.
66 A. Kaddouri, N. Dupont, P. Gelin and P. Delichere, *Catal. Lett.*, 2011, **141**, 1581.
67 K. Yoshida, C. Gonzalez-Arellano, R. Luque and P. L. Gai, *Appl. Catal., A*, 2010, **379**, 38.
68 X. Xu, J.-W. He and D. W. Goodman, *Surf. Sci.*, 1993, **284**, 103.
69 O. P. Tkachenko, K. V. Klementiev, M. W. E. van den Berg, H. Gies and W. Grünert, *Phys. Chem. Chem. Phys.*, 2006, **8**, 1539.
70 O. P. Tkachenko, K. V. Klementiev, N. Koc, X. Yu, M. Bandyopadhyay, S. Grabowski, H. Gies and W. Grünert, *Stud. Surf. Sci. Catal.*, 2004, **154**, 1670.
71 G. Moretti, C. Dossi, A. Fusi, S. Recchia and R. Psaro, *Appl. Catal., B*, 1999, **20**, 67.
72 C. J. G. Van Der Grift, A. Mulder and J. W. Geus, *Appl. Catal.*, 1990, **60**, 181.
73 A. B. Gaspar, J. L. F. Brito and L. C. Dieguez, *J. Mol. Catal. A: Chem.*, 2003, **203**, 251.
74 G. Calleja, J. Aguado, A. Carrero and J. Moreno, *Appl. Catal., A*, 2007, **316**, 22.
75 X. Zhao and X. Wang, *J. Mol. Catal. A: Chem.*, 2007, **261**, 225.
76 P. Michorczyk, J. Ogonowski, P. Kuśtrowski and L. Chmielarz, *Appl. Catal., A*, 2008, **349**, 62.
77 M. Trejda, A. Wojtaszek, M. Ziolek and J. Kujawa, *Appl. Catal., A*, 2009, **365**, 135.
78 G. Wang, L. Zhang, J. Deng, H. Dai, H. He and C. T. Au, *Appl. Catal., A*, 2009, **355**, 192.
79 R. Zhang, D. Shi, Y. Zhao, B. Chen, J. Xue, X. Liang and Z. Lei, *Catal. Today*, 2011, **175**, 26.
80 L. Mahoney, C.-M. Wu, H. S. Kibombo, E. Thiruppathi, J. Baltrusaitis, S. Rasalingam and R. T. Koodali, *Microporous Mesoporous Mater.*, 2012, **170**, 211.
81 K. Pelzer, J.-P. Candy, G. Godard and J.-M. Bassetpag, in *Nanoparticles and catalysis*, ed. D. Astruc, Wiley-VCH Verlag GmbH & Co KGaA, Weinheim, 2008, vol. 1, p. 613.
82 http://www.webelements.com/chromium/compounds.html.
83 C. H. Tu, A. Q. Wang, M. Y. Zheng, X. D. Wang and T. Zhang, *Appl. Catal., A*, 2006, **297**, 40.
84 X. C. Zheng, S. H. Wu, S. P. Wang, S. R. Wang, S. M. Zhang and W. P. Huang, *Appl. Catal., A*, 2005, **283**, 217.
85 Z. Liu, M. D. Amiridis and Y. J. Chen, *J. Phys. Chem. B*, 2005, **109**, 1251.
86 F. Delbecq and P. Sautet, *J. Catal.*, 1995, **152**, 217.